Carla M. Uribe-Rincón, Thorsten M. Gesing and Mohammad Mangir Murshed*

Synthesis of schafarzikite-type (PbBi)($Fe_{1-x}Mn_x$)O_4: a study on structural, spectroscopic and thermogravimetric properties

https://doi.org/10.1515/zkri-2025-0023
Received May 24, 2025; accepted June 4, 2025;
published online June 23, 2025

Abstract: In the mineral schafarzikite ($FeSb_2O_4$) the stereochemical active $5s^2$ lone electron pairs (LEPs) play pivotal roles to diverse crystal-physico-chemical properties. The complete substitution of Sb(III) with an equivalent amount of Pb(II) and Bi(III) leads to higher oxidation state of the transition element (e.g., Fe^{3+}) and offers a mixed stereochemical activity of the $6s^2$ LEPs. Here we report the synthesis and characterization of a solid solution (PbBi)($Fe_{1-x}Mn_x$)O_4 (x = 0–1.0; Δx = 0.1). The polycrystalline samples are synthesized in sealed quartz tubes at 923 K and a pressure of about 1.0 Pa. The crystal structure of each member of the solid solution has been analyzed by X-ray power diffraction data Rietveld refinements. The metric and the geometric parameters (bond lengths, angles, distortion of the polyhedra) have been followed with respect to the chemical composition. The Wang-Liebau eccentricity (WLE) parameter, which measures the strength of the stereochemical activity, has been found to be associated with the over-bonding nature of the LEP cations. The vibrational properties are characterized using Raman and infrared spectroscopy, supporting the structural features. The optical band gap is evaluated from the UV/Vis diffuse reflectance spectra using both conventional Tauc's and derivation of absorption spectrum fitting (DASF) methods. This study particularly highlights the miscibility between Fe(III) and Mn(III) cations on a single Wyckoff site within the schafarzikite-type structures, where the LEP driven void channels seem to be more suitable for a small cation (e.g., Li^+) insertion than the mineral schafarzikite.

Keywords: schafarzikite; lone electron pair; crystal structure; optical phonon; band gap

***Corresponding author: Mohammad Mangir Murshed**, University of Bremen, Institute of Inorganic Chemistry and Crystallography, Leobener Straße 7, D-28359 Bremen, Germany; and University of Bremen, MAPEX Center for Materials and Processes, Bibliothekstraße 1, Universität Bremen, D-28359 Bremen, Germany, E-mail: murshed@uni-bremen.de. https://orcid.org/0000-0002-9063-372X
Carla M. Uribe-Rincón, University of Bremen, Institute of Inorganic Chemistry and Crystallography, Leobener Straße 7, D-28359 Bremen, Germany. https://orcid.org/0009-0008-8486-6376
Thorsten M. Gesing, University of Bremen, Institute of Inorganic Chemistry and Crystallography, Leobener Straße 7, D-28359 Bremen, Germany; and University of Bremen, MAPEX Center for Materials and Processes, Bibliothekstraße 1, Universität Bremen, D-28359 Bremen, Germany. https://orcid.org/0000-0002-4119-2219

1 Introduction

While the mineral schafarzikite ($FeSb_2O_4$) has been known since 1921,[1] the isostructural Mn-containing mineral manganoschafarzikite ($MnSb_2O_4$)[2] was discovered very recently. For a general description, the chemical composition can be written either as ML_2O_4 with M^{2+} and L^{3+} cations, where L represents elements with stereochemically active lone electron pairs (LEPs), or as L_2MO_4 with L^{2+}, L^{3+} and M^{3+}. The crystal structure can be described as mullite-type,[3] where the edge-sharing MO_6 octahedra chains run along the c-axis, as shown in Figure 1.

The L_2MO_4 mullite-type O8 phases ($L_4M_2O_8$),[4–8] where the L-cation (e.g., Pb^{2+}, Sb^{3+}, Bi^{3+}) keeps a stereochemically active ns^2 LEP located at the apex of a distorted LO_3E nido-like tetrahedron (LEP = E) that connects the MO_6 octahedra of the respective chains. The E lobes expose as pseudo-ligands, producing a negatively charged void channel along the c-axis. This LEP-driven quasi-1D channel draws particular attention in designing functional energy materials. For instance, the LEP induced void space in $MnSb_2O_4$,[9] $CoSb_2O_4$ and $NiSb_2O_4$[10] are demonstrated as potential anode candidates for Li-ion batteries. Moreover, $FeSb_2O_4$[11] has been shown to be a suitable host for fluoride (F^-) inclusion. The reversible topochemical fluoride was inserted into the quasi-1D tunnels (Figure 1) followed by Fe^{2+}/Fe^{3+} redox process along with the consequent lattice volume expansion/contraction. During the $Fe^{2+}\rightarrow Fe^{3+}$ oxidation, the $5s^2$ LEPs interact with the F-2p states, forming a larger SbO_3EF coordination environment, however, with relatively weak Sb–F bonds.[11]

The strength of the stereochemical activity of the LEPs essentially stabilizes the channel, which can be measured by the Wang-Liebau eccentricity (WLE) parameter. This scalar

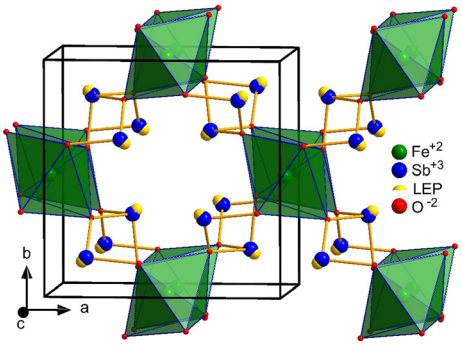

Figure 1: Crystal structure of $FeSb_2O_4$, showing the edge-sharing FeO_6 octahedra chains and the distorted tetrahedral SbO_3E coordination ($E = 5s^2$ active lone electron pair). The E lobes (yellow extension of the Sb atoms) form a quasi-1D channel along the c-axis.

quantity is found to be a function of the structural bond valence sum (BVS) of the LEP cations.[12–15]

Earlier attempts to study a solid solution of $(M'_{1-x}M''_x)L_2O_4$ included partial or full substitution of the M cation to tailor the endmember properties. Using ^{57}Fe Mössbauer spectroscopy Berry et al.[16] demonstrated that when Mg^{2+} substantially replaces Fe^{2+} the non-magnetic MgO_6 subunit disrupts the magnetic exchange interactions between the Fe^{2+} cations along the c-axis, and a composition of $(Fe_{0.25}Co_{0.75})Sb_2O_4$ shows a different antiferromagnetic (AFM) exchange between Fe^{2+} and Co^{2+} than those of the endmembers. Cumby et al.[17] reported $(Co_{1-x}Mn_x)Sb_2O_4$ and $(Co_{1-x}Fe_x)Sb_2O_4$ solid solutions, where the canted AFM structure gradually changes from C-type to A-type with increasing Co content due to rotation of the magnetic moment vectors from **c**- to **a**-direction. Within a MO_6 octahedra chains the direct exchange promotes an AFM ground state while a 90° super-exchange favors a ferromagnetic (FM) ordering between two neighboring M cations.[17] For co-sharing the 4*d* Wyckoff site by two magnetic cations, the relative magnitude of the exchange interactions plays pivotal roles for the magnetic orderings. Within the solid solution $(Mn_{1-x}V_x)Sb_2O_4$ a FM ordering is found for $0 < x \leq 0.6$. Clearly, the chemical tailoring of the L and M sites can significantly influence the physical properties.[18–22] Introducing Pb^{2+} into $FeSb_2O_4$ results in partial oxidation of Fe^{2+} to Fe^{3+} in $Fe(Sb_{1-x}Pb_x)_2O_4$.[23] As such, the Néel temperature (T_N) increases from 45 K ($FeSb_2O_4$) to 69 K ($FeSb_{1.4}Pb_{0.6}O_4$) and the parental A-type AFM turns into C-type AFM ordering. Complete substitution of Sb^{3+} by mixed valence L-type cations has recently been published[24] for two new members of the schafarzikite-type family: $(PbBi)FeO_4$ keeps the parental A-type AFM ordering at T_N of 24 K and $(PbBi)MnO_4$ a G-type AFM at T_N of 43 K. Therefore, it is worth testing whether a complete miscibility exists between Fe^{3+} and Mn^{3+} within the solid solution $(PbBi)(Fe_{1-x}Mn_x)O_4$, which eventually offers a systematic study to follow the crystal chemical properties.

2 Experimental

2.1 Synthesis

Polycrystalline samples of $(PbBi)(Fe_{1-x}Mn_x)O_4$ ($x = 0$–1) were synthesized by the conventional solid-state method, grinding respective stoichiometric amounts of PbO (99.9 %, Alfa Aesar), Bi_2O_3 (99 %, Alfa Aesar), Fe_2O_3 (99 %) and Mn_2O_3 (99 %) in a agate mortar. Afterward, the mixture was pressed into pellets and transferred into dried quartz tubes. The tubes were sealed with an internal pressure of about 1.0 Pa followed by heating in a muffle furnace at 923 K for 72 h.

2.2 X-ray powder diffraction

X-ray powder diffraction (XRPD) data were collected on a Bruker D8 Advance diffractometer (Bruker AXS GmbH, Karlsruhe Germany) using a Bragg-Brentano geometry with $CuK_{\alpha 1}$ radiation and a Johansson monochromator. Measurements were taken at ambient conditions from 10° to 130° 2θ with a step width of 0.0145° and a data collection time of 1.25 s per step. The XRPD data were refined using the Rietveld method (TOPAS V4.2, Bruker AXS). The respective fundamental parameters were calibrated using a LaB_6 standard and used for the profile line-shape. During the refinements general parameters such as sample displacement, scale factor and background parameter (Chebychev polynomial) were optimized. The lattice parameters, atomic coordinates and atomic displacement parameters were also refined. The isotropic atomic displacement parameters (ADP) were constrained between atoms located at the same Wyckoff site (Bi/Pb, Fe/Mn) to avoid unphysical outcomes such as negative ADPs. Besides the heavy elements Pb and Bi, the ADPs of the light oxygen atoms were as well refined constrained to each other. The starting atomic coordinates were taken from the crystal structure data of $FeSb_2O_4$, where the 8*h* Wyckoff site was set to co-share between Pb^{2+} and Bi^{3+} with an occupancy of 0.5 each.[25] Since the X-ray scattering factors of Pb^{2+} and Bi^{3+} are similar, the Rietveld refinement cannot distinguish the occupancy parameters between the respective atoms. As such, the nominal compositional occupancy was fixed, which was supported by the EDX results. For the same

reason, the occupancy parameter between Fe and Mn were set to their nominal compositions.

2.3 UV/Vis diffuse reflectance spectroscopy

A Shimadzu UV-2600 (Shimadzu, Kyoto, Japan) spectrophotometer, equipped with an ISR-2600 plus two-detector integrating sphere (Pike Technologies, USA), was used for the collection of optical diffuse reflectance spectra at room temperature. Data were recorded in the wavelength range between 190 nm and 950 nm with a step of 1 nm. A $BaSO_4$ powder sample was used as reference standard for the baseline correction. The Tauc-type[26,27] band gaps (direct or indirect) were compared with those determined by the DASF method[28,29] after converting the reflection data to absorption ones using the Kubelka-Munk transformation.[30]

2.4 Vibrational spectroscopy

Raman spectra were recorded on a LabRam ARAMIS (Horiba Jobin–Yvon) Micro-Raman spectrometer. A laser of 525 nm providing power of less than 20 mW was focused on the sample surface through a 50× objective (Olympus) with a numerical aperture of 0.75. The focus spot was estimated to be about 1 µm when closing the confocal hole to 200 µm. Using a backscattering geometry each spectrum was recorded between 40 cm^{-1} and 850 cm^{-1} with a spectral resolution of approx. 3.2 cm^{-1} using a grating of 1800 grooves/mm and a thermoelectrically cooled CCD detector (Synapse, 1024 × 256 pixels). Fourier transform infrared (FTIR) spectra were collected in the mid-infrared range from 400 cm^{-1} to 4000 cm^{-1} on a Bruker VERTEX 80v spectrometer equipped with a DTGS Detector. Standard KBr pellet method was used for data collection.

2.5 Thermal analysis

Simultaneous thermogravimetric analysis and differential scanning calorimetry (TGA/DSC) measurements were performed on a simultaneous TGA/DSC 3+ STAR e system (Mettler Toledo, Schwerzenbach, Switzerland). Approximately 10 mg of each polycrystalline sample was measured with a heating rate of 10 K/min and a continuous N_2 flow of 20 mL/min from 300 K to 1500 K. An empty corundum crucible was used as reference. Data were normalized to the respective mass and a drift correction was applied based on empty crucible versus empty crucible data.

3 Results and discussion

3.1 Crystal structure

XRPD data Rietveld refinements confirm that each member of the $(PbBi)(Fe_{1-x}Mn_x)O_4$ solid solution is found to be phase pure and crystallizes in the space group $P4_2/mbc$. A representative Rietveld plot of $(PbBi)(Fe_{0.5}Mn_{0.5})O_4$ is shown in Figure 2 and the refined crystal structural parameters of the solid solution $(PbBi)(Fe_{1-x}Mn_x)O_4$ are given in Table S1 (Supplementary information). The metric parameters ($a = b$, c and V) are given in Table S2, and the interatomic bond distances and angles in Table S3.

Complete substitution of Fe^{3+} with Mn^{3+} in $(PbBi)(Fe_{1-x}Mn_x)O_4$, leads to a slight elongation (0.3(1) %) of the (a, b)- and a contraction (−0.7(2) %) of the c-lattice parameters. The latter parameter plays the dominant role for almost a negligible cell volume contraction of −0.1(4) % between the endmembers, as depicted in Figure 3. The observed cell volumes of the endmembers $(PbBi)FeO_4$ ($V = 441.35(4)\cdot10^6$ pm^3) and $(PbBi)MnO_4$ ($V = 440.76(6)\cdot10^6$ pm^3) are in excellent agreement with the reported ones.[24,31] The slight deviation of each lattice parameter from the Vegard's rule line can be understood due to these small changes of the metric parameters with respect to the chemical composition. The interplay between the geometric distortion of the MO_6 and LO_3E polyhedra and the stereochemical activities of the associated LEPs should also be considered to explain the slight deviation from the Vegard's lines. Moreover, the adoption of the high-spin (HS) and low-spin (LS) configurations of the M cations directly influence the respective ionic radii, and the metric parameters as well. Due to Fe^{3+}/Mn^3 mixed occupancy the average ionic radius of the M cations should consider four different spin configurations: Fe^{3+}/Mn^{3+} (LS–LS), Fe^{3+}/Mn^{3+} (LS–HS), Fe^{3+}/Mn^{3+} (HS–LS) and Fe^{3+}/Mn^{3+}

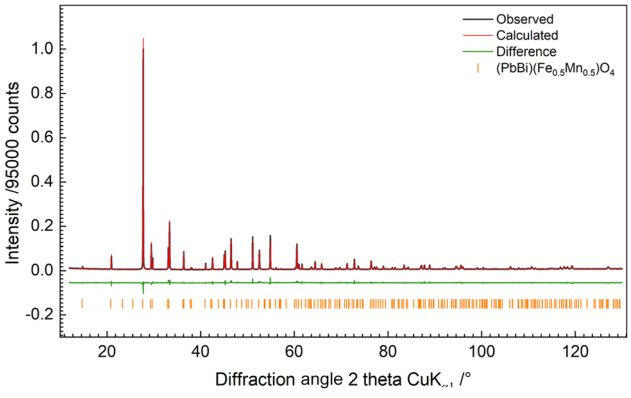

Figure 2: Rietveld plot of $(PbBi)(Fe_{0.5}Mn_{0.5})O_4$ schafarzikite-type sample.

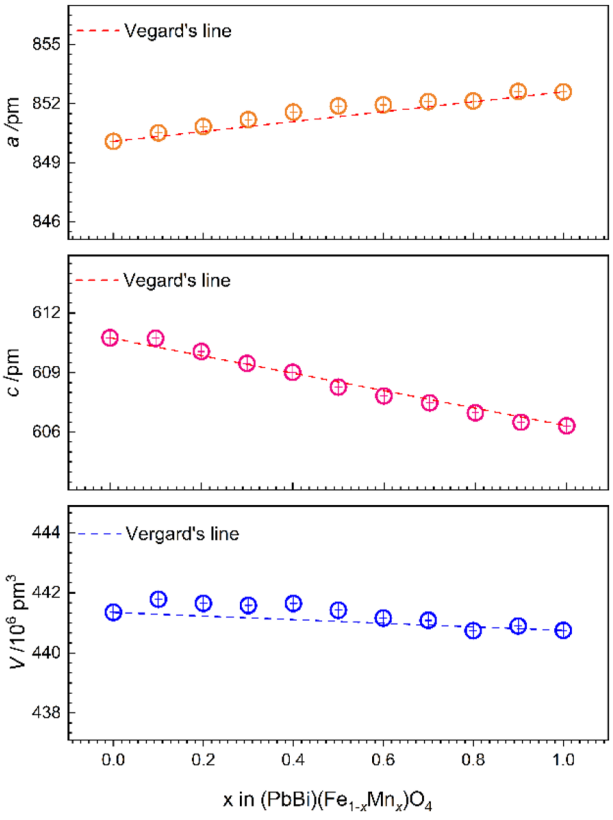

Figure 3: Changes of the metric parameters in $(PbBi)(Fe_{1-x}Mn_x)O_4$ with respect to the *x*-value of the chemical composition.

(LS–LS). The trends of the metric parameters fit well to the Fe^{3+}/Mn^{3+} (LS–HS) configuration (Figure S2).

The axial Fe–O1 (202.8(11) pm) and equatorial Fe–O2 (203.8(7) pm) bond lengths for the endmember $(PbBi)FeO_4$ are found to be close (Table S3) to the respective Mn–O1 (200.0(7) pm) and Mn–O2 (200.2(7) pm) bond lengths in $(PbBi)MnO_4$. Due to mixed occupancy the axial (Fe/Mn)–O1 and the equatorial (Fe/Mn)–O2 bond distances lie close to each other irrespective to the chemical composition, as depicted in Figure 4.

The gradual decrease of the *M*–*M* distance from 305.3(8) pm (Fe–Fe) to 303.1(6) pm (Mn–Mn) in the octahedral chains can be understood from the deviation between the Fe–O and Mn–O distances, which leads to a contraction of the *c*-lattice parameter. The MO_6 octahedral volume remains almost constant at $10.94(4)\cdot10^6$ pm^3 followed by a sharp contraction for $x = 1.0(10.42(6)\cdot10^6$ pm$^3)$ (Figure 4), indicating a dominant influence of the Fe^{3+} cations in the structure. The underlying geometric consequences should influence the polyhedral distortions. The mixed valence LEP cations (Pb^{2+} and Bi^{3+}) on the same atomic position imposes additional distortion to the LO_3E tetrahedra[32] due to the asymmetric distribution of the O–Pb–O–Bi–O distances. Indeed, the bond distortion in the LO_4E polyhedra shows a slight increase, with an insignificant change of the MO_6 polyhedra, for an increasing Mn content in the solid solution (Figure S1).

The bond valence sum of the *M*- and *L*-cations are calculated from the *M*–O and *L*–O bond distances (Table S3) in the MO_6 and LO_3 polyhedra, respectively, for any given chemical composition.[33,34] The structural BVS of the *L*-cation exhibits an over-bonding nature above the average 2.5 v.u., as shown in Figure 5, which is a common finding for stereochemically active LEP containing cations.[14,15] On the other hand, except for the endmember $(PbBi)MnO_4$ where Mn shows a BVS of 2.65(4) v.u., the BVS of the M^{3+} cation shows an under-bonding nature below the formal value 3 v.u. with almost a constant deviation of about 0.2 v.u. throughout the solid solution. Such a constant deviation may not be explained due to experimental uncertainty. Since all oxygen atoms of the LO_3E polyhedra are linked to the MO_6 octahedral apexes, the respective BVS deviations in opposite directions can be understood from geometric distortions. The observed absolute value of the WLE parameters ($|\mathbf{\Phi}_i|$) of $3.72(2)\cdot10^{-5}$ and $3.43(2)\cdot10^{-5}$ for $(PbBi)FeO_4$ and $(PbBi)MnO_4$, respectively, are within the typical range of a stereochemically active Pb^{2+}/Bi^{3+} cations in the crystal structures.[14] Most of the $|\mathbf{\Phi}_i|$ values lie close to $3.75\cdot10^{-5}$, indicating an asymmetric distribution of the LEP[35] followed by a withdrawal of the positive charge of the nucleus toward the bonding oxygen ligands. Such redistribution leads to an increase in the bonding capacity of an *L*-cation, which may extend the first coordination sphere[36] along with a higher coordination

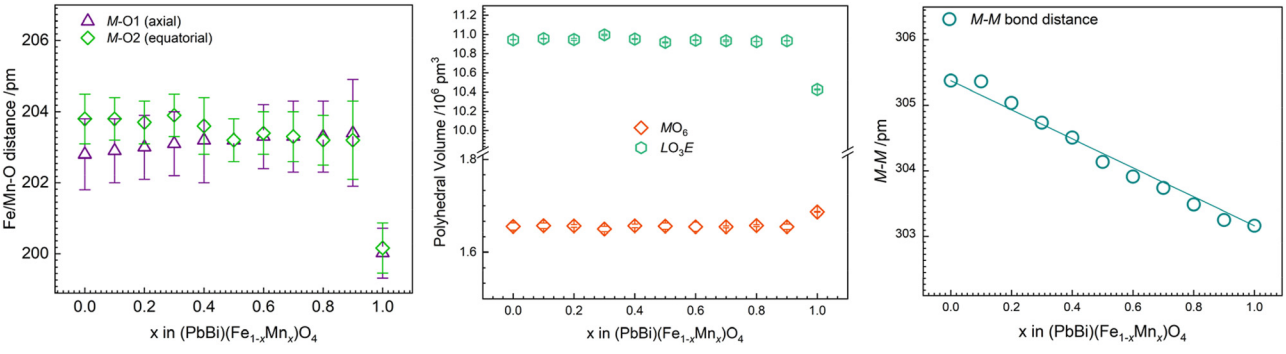

Figure 4: Fe/Mn–O interatomic bond distances (left), polyhedral volumes (middle) and *M*–*M* distances with respect to chemical composition in $(PbBi)(Fe_{1-x}Mn_x)O_4$. The solid line is for eye guideline.

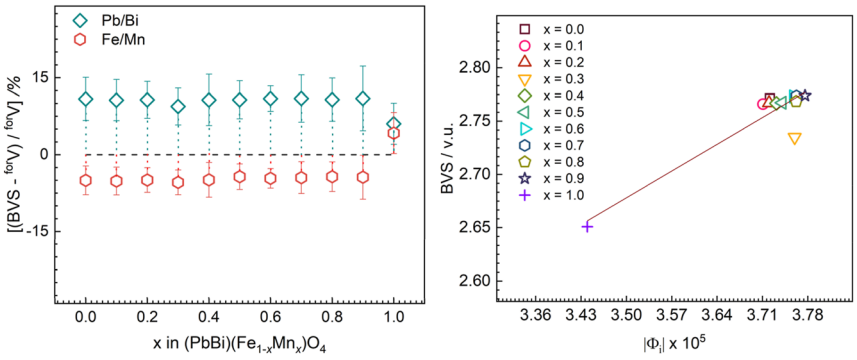

Figure 5: Deviations of bond valence sum (BVS) from formal valence (^{for}V) of the *M* and *L*-cations in (PbBi)($Fe_{1-x}Mn_x$)O_4 (left), and the correlation between the absolute value of the Wang-Liebau eccentricity parameter ($|\Phi_i|$) and the BVS for Pb/Bi (right).

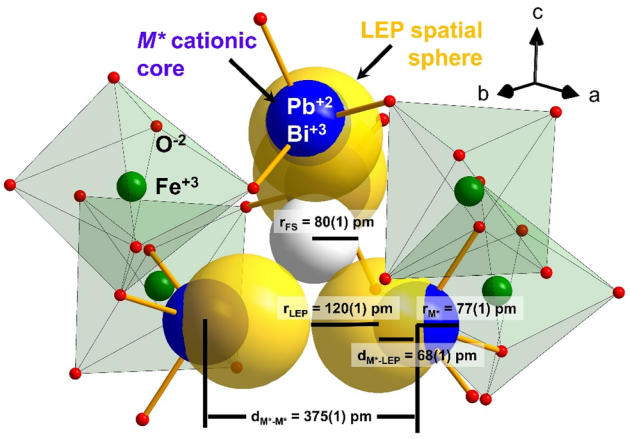

Figure 6: Schematic representation for the estimation of effective free space in the (PbBi)FeO_4 schafarzikite structure using Hamani[37] model, where the *L*-cation is decomposed into a cationic core (*M**) and a LEP spatial sphere with radii of r_{M*} and r_{LEP}, respectively, and $d_{M*\text{-}LEP}$ is the distance between their centers. The free space sphere with a radius of r_{FS} is located at the center of a pseudo-tetrahedron formed by four LEP cations, which fits well for small cations such as lithium.

number. This phenomenological concept can further explain the inclusion of Li^+ cations into the schafarzikite void channels.[11] According to the Hamani LEP localization model[37] where each *L*-cation is decomposed into cationic cores (*M**) and LEP spatial spheres, as given in Figure 6, allowing for the calculation of the distance between *M** and center of the LEP sphere ($d_{M*\text{-}LP}$). Irrespective of the chemical composition throughout the solid solution the LEP sphere radius of the Pb^{2+}/Bi^{3+} cations is found to be 120(1) pm and the center of the LEP sphere locates 68(1) pm away from the Pb^{2+}/Bi^{3+} core which itself possesses a radius of 77(1) pm. Since the shortest interatomic distance between two LEP cations is 375 pm, the estimated corresponding LEP-LEP distance of about 239(1) pm (375 pm – 2*68(1) pm = 239(1) pm) well allows free space in the center of a pseudo-tetrahedron formed by four LEP cations, for a sphere with a radius of ~80 pm. Such empty space well fits, for instance, to the cationic diameter of lithium of 118 pm.[38,39]

3.2 Vibrational properties

For the room-temperature Raman and FTIR spectra of (PbBi)($Fe_{1-x}Mn_x$)O_4, which are given in Figure 7, the factor group analysis predicts 62 vibrational modes ($5A_{1g} + 3A_{1u} + 7A_{2g} + 5A_{2u} + 7B_{1g} + 5B_{1u} + 5B_{2g} + 3B_{2u} + 13E_u + 9E_g$). As listed in Table S4, 26 of them are Raman ($5A_{1g} + 7B_{1g} + 5B_{2g} + 9E_g$), 16 are infrared ($4A_{2u} + 12E_u$) active, 2 are acoustic ($A_{2u} + E_u$) and a substantial number of 18 of them are optically silent ($3A_{1u} + 7A_{2g} + 5B_{1u} + 3B_{2u}$). Fitting the resolved Raman spectra requires 19 and 17 pseudo-Voigt peaks for the endmembers (PbBi)FeO_4 and (PbBi)MnO_4, respectively. The vibrational features of each Raman spectrum can be categorized into three spectral regions of low- (<140 cm^{-1}), mid- (140–600 cm^{-1}) and high-frequency (>600 cm^{-1}).

The low-frequency region is mainly dominated by the *L*–O–*L* and O–*L*–O bending contributions of the LO_4E nido-tetrahedra. The mid-range covers the *M*–O–*M* and O–*M*–O bending of the MO_6 octahedra, and the *L*–O stretching modes of LO_4E polyhedra. The high-frequency region is purely associated with the *M*–O symmetric and asymmetric vibrations in the MO_6 octahedra. More details of the vibrational description of the endmember (PbBi)MnO_4 are available elsewhere.[24] The low-frequency Raman modes at 106(1) cm^{-1} and 134(1) cm^{-1} of (PbBi)FeO_4 gradually shift to 95(2) cm^{-1} and 130(1) cm^{-1}, respectively, as shown in Figure S3, which is mainly due to weaking of the associated bending force constant as the average *L*-O bond distances between the endmembers (Table S3) does not significantly change. Some high-frequency modes show slight blue shifts, indicating to the observed shortening of the *M*–O bond lengths in the MO_6 octahedra. To better understand the vibrational spectra of the centrosymmetric structures the FTIR spectra of the investigated phases provide complementary information (Figure S4). The compact nature of the FTIR spectra due to merging and the instrumental limitation (>400 cm^{-1}), the shift of the mode frequencies could hardly be followed with changing chemical composition of the solid solution. However, an apparent

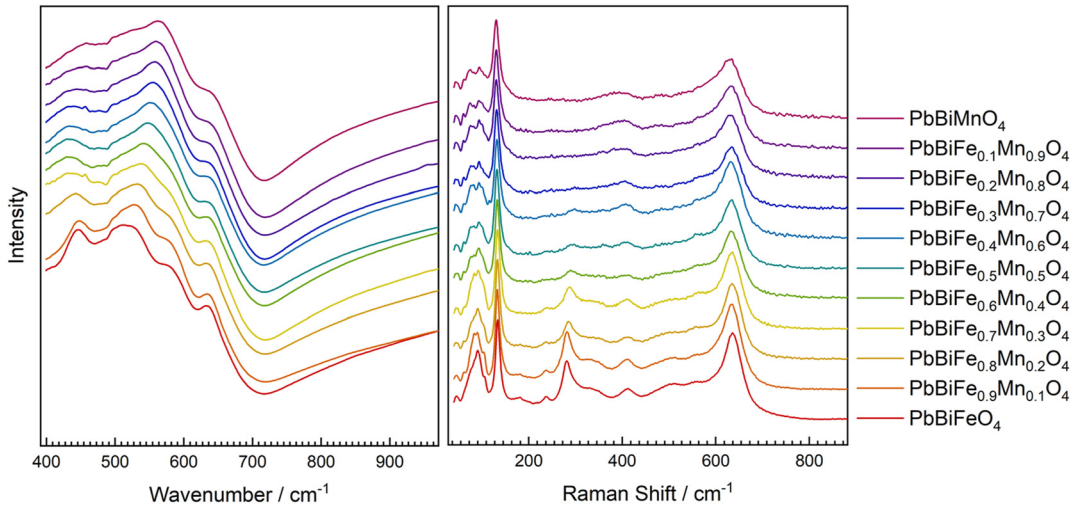

Figure 7: Stack plots of FTIR (left) and Raman (right) spectra of (PbBi)($Fe_{1-x}Mn_x$)O_4.

quasiharmonic trend of each FTIR peak maximum complements the mid- and high-frequency Raman modes.

3.3 Optical band gap

The UV/Vis diffuse reflectance spectra of the endmembers of the (PbBi)($Fe_{1-x}Mn_x$)O_4 solid solution are shown in Figure S5 and Figure S6. To determine the optical band-gap transition energy (E_g) from a given absorption spectra by using the Tauc method,[27] the reflectance data are transformed into the corresponding absorption spectra using the Kubelka-Munk function.[40] Absorption data are then recalculated for the use of the Tauc method to calculate a band-gap transition energy assuming a direct (E_d) or indirect (E_i) electron transition. Each analysis is performed by plotting a tangent to the baseline at low energies and a second tangent to the slope in the linear region of the absorption onset.[41–43] The energy of the band gap can then be estimated by the intersection of these two lines (Figure S5). Since the Tauc method cannot assert the nature of the transition type (E_d or phonon assisted E_i), the derivative absorption spectra fitting (DASF) method[28] is demonstrated[29,44] to compare the optical band-gap types. With gradual increase of Mn content in the solid solution the reflectivity becomes noticeably lower, which hampers calculating the band-gap energies using Tauc's approach. However, data treated with the DASF method appears as peak shape (Figure S5), allowing for calculation of the band-gap energy (E_g) from the fitted peak-maximum. A comparison between E_d and E_i with the DASF E_g value guides to ascertain the type of transition. In the present, since each band-gap energy obtained by the DASF method (Table S5) agrees well with E_d, each member of the solid solution presumably follows direct transition. Beside the band-gap energy, the *FWHM* (F_g) of the DASF line shape essentially describes the edge of the valence and the conduction bands split into different quantized levels based on the distribution of crystallite sizes and available defects. If one assumes the slope of the absorption edge corresponds directly to the sharpness of the transition (the shaper the energy level separation the flatter the valence and/or the conduction bands in the transition region), the F_g of the DASF peak is a direct measure for this behavior. Although the optical band gaps of the schafarzikite family members are not well explored, the experimental E_g of minium Pb_3O_4 (2.1 eV)[45] and $MnSb_2O_4$ (2.65(2) eV)[9] are comparable to those of the present compounds. Considering the direct transition (PbBi)FeO_4 holds a band gap of 2.24(3) eV which drops to 1.77(3) eV for x = 0.3. Afterward, a slight linear decrease results in 1.72(3) eV for the endmember (PbBi)MnO_4, as shown in Figure 8.

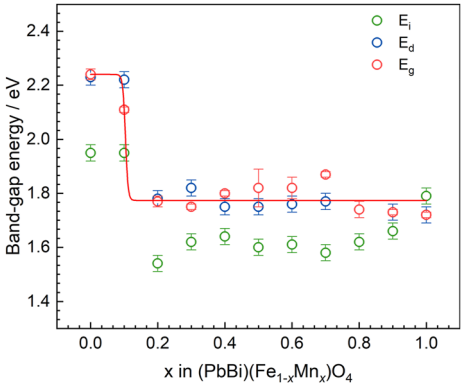

Figure 8: Changes of direct (E_d) and indirect (E_i) electron transfer to the conduction band and band-gap energy (E_g) with respect to the chemical composition x in (PbBi)($Fe_{1-x}Mn_x$)O_4.

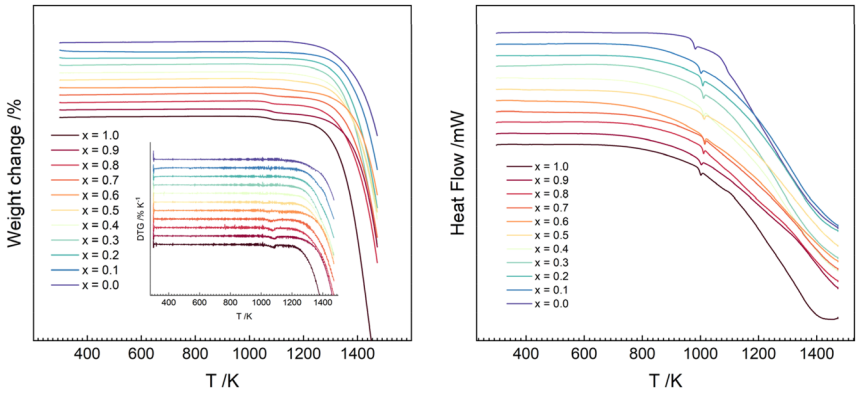

Figure 9: Thermoanalytic evaluation of $(PbBi)(Fe_{1-x}Mn_x)O_4$.

3.4 Thermal properties

The TG and the DSC stack plots of the compounds $(PbBi)(Fe_{1-x}Mn_x)O_4$, as shown in Figure 9, suggest that samples with higher Mn content exhibit ~1 % weight loss at around 1080(3) K, 1084(1) K, 1075(3) K, and 1062(1) K, respectively, for x = 0.7, 0.8, 0.9 and 1.0. Such tiny weight loss is most likely associated with the evaporation of Bi-containing amorphous contents. Exothermic signals are observed at 981(1) K and 1000(1) K, respectively, for the endmembers $(PbBi)FeO_4$ and $(PbBi)MnO_4$. The other members ($0 < x < 0.7$) of the solid solution exhibit an exothermic signal at slightly lower temperatures. The onset temperature (first point of inflection) has been taken as the decomposition temperature, which fluctuates around 1360 K within 20 K for any given composition of the solid solution, as shown in Figure S7.

4 Conclusions

The solid solution of schafarzikite-type $(PbBi)(Fe_{1-x}Mn_x)O_4$ has been successfully synthesized. X-ray powder data Rietveld refinements confirm each member to be phase pure and to crystallizes in space group $P4_2/mbc$. According to Hume-Rothery rules [46] *stricto sensu* for intermetallics, the atomic size, the electro-chemical effect and the relative valency between Fe(III) and Mn(III) favor a complete miscibility for a given chemical composition. While the X-ray scattering factors can hardly distinguish between the cations in the same site (8*h*: Pb(II) and Bi(III); 4*d*: Fe(III) and Mn(III)), EDX based atomic content unambiguously supports the chemical composition. Both Raman and FTIR spectra complement the structural subunit arrangements. Since the spin-only magnetic moment differs between Fe^{3+} and Mn^{3+} along with their spin configurations (high-spin or low-spin), how the magnetic property changes with respect to the Fe^{3+}/Mn^{3+} in the solid solution leaves scopes for a future study. While incorporation of fluoride anion into the $FeSb_2O_4$ structure[11] leads to Fe^{2+}/Fe^{3+} redox process, the void space formed by the stereochemical active lone electron pairs of these tetragonal phases can be suitable for Li^+ insertion for an opposite M^{3+}/M^{2+} reversible conversions for designing energy materials.

Acknowledgments: The University of Bremen is cordially acknowledged for technical and administrative supports.
Research ethics: The local Institutional Review Board deemed the study exempt from review.
Informed consent: Informed consent was obtained from all individuals included in this study.
Author contributions: Carla M. Uribe-Rincón: drafting the article, acquisition of data, analysis and interpretation of data. Thorsten M. Gesing: conception and design of the study, analysis and interpretation of data, revising the manuscript critically for important intellectual contents. M. Mangir Murshed: conception and design of the study, analysis and interpretation of data, revising the manuscript critically for important intellectual contents.
Use of Large Language Models, AI and Machine Learning Tools: None declared.
Conflict of interest: The authors hereby state no conflict of interest.
Research funding: Deutsche Forschungsgemeinschaft (DFG) supporting the project within grant MU4415/3-1 (project-ID: 492161439) and DFG the funding of the IR spectrometer under grant number INST144/521-1FUGG.
Data availability: Data can be obtained upon request to the corresponding author.

References

1. Krenner, J. A. *Z. Kristallogr.* **1921**, *56*, 198–200.
2. Holtstam, D.; Langhof, J.; Friis, H.; Karlsson, A.; Erambert, M. *Eur. J. Mineral.* **2024**, *36*, 311–322.

3. Fischer, R. X.; Schneider, H.; Rahman, S.; Freimann, S. *Mullite*; Wiley VCH: Weinheim, 2005; pp. 1–70.
4. Murshed, M. M.; Gesing, T. M. *Acta Crystallogr. A* **2012**, *68*, s195.
5. Murshed, M. M.; Mendive, C. B.; Curti, M.; Nenert, G.; Kalita, P. E.; Lipinska, K.; Cornelius, A. L.; Huq, A.; Gesing, T. M. *Mater. Res. Bull.* **2014**, *59*, 170–178.
6. Gogolin, M.; Murshed, M. M.; Ende, M.; Miletich, R.; Gesing, T. M. *J. Mater. Sci.* **2020**, *55*, 177–190.
7. Gesing, T. M.; Mendive, C. B.; Curti, M.; Hansmann, D.; Nenert, G.; Kalita, P. E.; Lipinska, K. E.; Huq, A.; Cornelius, A. L.; Murshed, M. M. *Z. Kristallogr.* **2013**, *228*, 532–543.
8. Curti, M.; Mendive, C. B.; Bredow, T.; Mangir Murshed, M.; Gesing, T. M. *J. Phys.: Condens. Matter.* **2019**, *31*, 345701.
9. Roelsgaard, M.; Norby, P.; Eikeland, E.; Sondergaard, M.; Iversen, B. B. *Dalton Trans.* **2016**, *45*, 18994–19001.
10. Jibin, A. K.; Reddy, M. V.; Subba Rao, G. V.; Varadaraju, U. V.; Chowdari, B. V. R. *Electrochim. Acta* **2012**, *71*, 227–232.
11. Zaheer, W.; Andrews, J. L.; Parija, A.; Hyler, F. P.; Jaye, C.; Weiland, C.; Yu, Y.-S.; Shapiro, D. A.; Fischer, D. A.; Guo, J.; Velázquez, J. M.; Banerjee, S. *ACS Energy Lett.* **2020**, *5*, 2520–2526.
12. Liebau, F.; Wang, X. *Z. Kristallogr.* **2005**, *220*, 589–591.
13. Liebau, F.; Wang, X.; Liebau, W. *Chem. – Eur. J.* **2009**, *15*, 2728–2737.
14. Wang, X.; Liebau, F. *Acta Crystallogr. B* **1996**, *52*, 7–15.
15. Wang, F. L. X. *Z. Kristallogr.* **1996**, *211*, 437–439.
16. Berry, F. J.; de Laune, B. P.; Greaves, C.; Hah, H. Y.; Johnson, C. E.; Johnson, J. A.; Kamali, S.; Marco, J. F.; Thomas, M. F.; Whitaker, M. J. *Hyper. Interact.* **2018**, *239*, 8.
17. Cumby, J.; de Laune, B. P.; Greaves, C. *J. Mater. Chem. C* **2016**, *4*, 201–208.
18. Tiwari, A.; Kakarla, D. C.; Chen, W.-L.; Dhanasekhar, C.; Hu, Y.-J.; Lin, J.-Y.; Wang, C.-W.; Kuo, T.-W.; Pal, A.; Chou, M. M.-C.; Yang, H.-D. *Adv. Phys. Res.* **2024**, *3*, 2400056.
19. Fjellvåg, H.; Kjekshus, A.; Leskelä, T.; Leskelä, M.; Hoyer, E. *Acta Chem. Scand.* **1985**, *39*, 389–395.
20. de Laune, B. P.; Greaves, C. *J. Solid State Chem.* **2012**, *187*, 225–230.
21. de Laune, B. P.; Rees, G. J.; Whitaker, M. J.; Hah, H. Y.; Johnson, C. E.; Johnson, J. A.; Brown, D. E.; Tucker, M. G.; Hansen, T. C.; Berry, F. J.; Hanna, J. V.; Greaves, C. *Inorg. Chem.* **2017**, *56*, 594–607.
22. de Laune, B. P.; Rees, G. J.; Marco, J. F.; Hah, H. Y.; Johnson, C. E.; Johnson, J. A.; Berry, F. J.; Hanna, J. V.; Greaves, C. *Inorg. Chem.* **2017**, *56*, 10078–10089.
23. Whitaker, M. J.; Bayliss, R. D.; Berry, F. J.; Greaves, C. *J. Mater. Chem.* **2011**, *21*, 14523–14529.
24. Uribe-Rincón, C. M.; Ghosh, K.; Frederichs, T.; Gesing, T. M.; Murshed, M. M. *J. Solid State Chem.* **2025**, 125215.
25. Zemann, J. *Tschermaks Mineral. Petro. Mitt.* **1951**, *2*, 166–175.
26. Tauc, J. *Mater. Res. Bull.* **1968**, *3*, 37–46.
27. Tauc, J.; Grigorovici, R.; Vancu, A. *Phys. Stat. Solidi (b)* **1966**, *15*, 627–637.
28. Souri, D.; Tahan, Z. E. *App. Phys. B* **2015**, *119*, 273–279.
29. Kirsch, A.; Murshed, M. M.; Schowalter, M.; Rosenauer, A.; Gesing, T. M. *J. Phys. Chem. C* **2016**, *120*, 18831–18840.
30. Kubelka, F. P. A. M. *Z. Technische Phys.* **1931**, *12*, 593–601.
31. Wu, J.; Yan, X.; Lei, X.; He, L.; Guo, W.; Yan, S.; Kuang, X.; Yin, C. *J. Solid State Chem.* **2023**, *318*; https://doi.org/10.1016/j.jssc.2022.123770.
32. Halasyamani, P. S. *Chem. Mater.* **2004**, *16*, 3586–3592.
33. Brese, N. E.; O'Keeffe, M. *Acta Crystallogr. B* **1991**, *47*, 192–197.
34. Brown, I. D.; Altermatt, D. *Acta Crystallogr. B* **1985**, *41*, 244–247.
35. Murshed, M. M.; Rusen, A.; Fischer, R. X.; Gesing, T. M. *Mater. Res. Bull.* **2012**, *47*, 1323–1330.
36. Brandes, R.; Hoppe, R. *Z. Anorg. Allg. Chem.* **1994**, *620*, 1549–1558.
37. Hamani, D.; Masson, O.; Thomas, P. *J. App. Crystallogr.* **2020**, *53*, 1243–1251.
38. Shannon, R. D. *Acta Crystallogr. A* **1976**, *32*, 751–767.
39. Shannon, R. D.; Prewitt, C. T. *Acta Crystallogr. B* **1969**, *25*, 925–946.
40. Kubelka, P. *J. Opt. Soc. Am.* **1948**, *38*, 448–457.
41. M. M. R. Center; Department of Chemical Engineering, Stanford University, 2017. Available from: http://mmrc.caltech.edu.
42. Makuła, P.; Pacia, M.; Macyk, W. *J. Phys. Chem. Lett.* **2018**, *9*, 6814–6817.
43. Escobedo-Morales, R.-L. A.; Ruiz-Peralta, M. de L.; Tepech-Carrillo, L.; Sánchez-Cantú, M.; Moreno-Orea, J. E. *Heliyon* **2019**, *5*, e01505.
44. Teck, M.; Murshed, M. M.; Schowalter, M.; Lefeld, N.; Grossmann, H. K.; Grieb, T.; Hartmann, T.; Robben, L.; Rosenauer, A.; Madler, L.; Gesing, T. M. *J. Solid State Chem.* **2017**, *254*, 82–89.
45. Terpstra, H. J.; De Groot, R. A.; Haas, C. *J. Phys. Chem. Solids* **1997**, *58*, 561–566.
46. Hume-Rothery, W.; Smallman, R. E.; Haworth, C. W. *The Structure of Metals and Alloys*; Metals & Metallurgy Trust: London, 1969.

Supplementary Material: This article contains supplementary material (https://doi.org/10.1515/zkri-2025-0023).